Journal of Alloys and Compounds 702 (2017) 327–337

Contents lists available at ScienceDirect

Journal of Alloys and Compounds

journal homepage: http://www.elsevier.com/locate/jalcom

Combined theoretical and nanoscale experimental study of Pb(Ca,Ba)TiO_3, Pb(Sr,Ba)TiO_3, and Pb(Sr,Ca)TiO_3 complex perovskite structures: An investigation of the ferroelectric and electronic properties

D.S.L. Pontes [a], W.B. Bastos [d], A.J. Chiquito [b], E. Longo [a, d], F.M. Pontes [c, *]

[a] LIEC – CDMF- Department of Chemistry, Universidade Federal de São Carlos, Via Washington Luiz, Km 235, P.O. Box 676, 13565-905, São Carlos, São Paulo, Brazil
[b] NanO LaB – Department of Physics, Universidade Federal de São Carlos, Via Washington Luiz, Km 235, P.O. Box 676, 13565-905, São Carlos, São Paulo, Brazil
[c] Department of Chemistry, Universidade Estadual Paulista - Unesp, P.O. Box 473, 17033-360, Bauru, São Paulo, Brazil
[d] LIEC- CDMF-Institute of Chemistry, Universidade Estadual Paulista – Unesp, Araraquara, São Paulo, Brazil

ARTICLE INFO

Article history:
Received 21 November 2016
Received in revised form
17 January 2017
Accepted 22 January 2017
Available online 25 January 2017

Keywords:
Perovskite
Piezoresponse force microscopy
First-principles calculations
Thin films

ABSTRACT

Combined experimental and first-principles studies have been conducted to obtain a fundamental understanding of the effect of A-site chemical doping on the electronic structure and ferroelectric behavior of Pb(Ca,Ba)TiO_3, Pb(Sr,Ba)TiO_3, and Pb(Sr,Ca)TiO_3 perovskite complex solid solutions. Rietveld refinement of powder X-ray diffraction data shows that the crystal structure of all the three compounds is distorted from the ideal cubic perovskite structure. At the nanoscale, piezoresponse force microscopy (PFM) studies show low-performance ferroelectric properties of Pb(Sr,Ca)TiO_3 thin films when compared to Pb(Ca,Ba)TiO_3 and Pb(Sr,Ba)TiO_3 films. Theoretical analysis of the electronic band structure performed on the basis of density functional theory (DFT) allows to elucidate the origin of the different ferroelectric behaviors observed in Pb(Ca,Ba)TiO_3, Pb(Sr,Ba)TiO_3, and Pb(Sr,Ca)TiO_3 thin films. DFT-based computational calculations reveal that there is a strong correlation between the effects of Ti 3d non-bonding orbitals (responsible for π Ti–O bonding) and the ferroelectric polarization behavior of A(A′A″)BO_3 complex perovskite solid solutions. In our study, very low Ti $3d_{xy}$, d_{xz}, and d_{yz} non-bonding electronic density state contributions were observed and the presence of mainly ionic Ca–O and Sr–O bonds. These effects are the reason for the unusually weak polarization, low tetragonality, and poor ferroelectricity of Pb(Sr,Ca)TiO_3 thin films. This is in contrast to the observed behaviors of Pb(Ca,Ba)TiO_3 and Pb(Sr,Ba)TiO_3 thin films. However, our first-principles calculations agree well with the PFM-based experimental results obtained in the nanometer scale.

1. Introduction

Notably intense global research has been directed toward the exhaustive study of the wide spectrum of properties (ferroelectricity, piezoelectricity, sensors, ferromagnetism, photocatalysis, and photovoltaics) of inorganic and hybrid organic-inorganic perovskites classes [1–5]. Previous studies have demonstrated that the increasing capabilities of first-principles calculations and the advances in characterization techniques in the nanoscale range have become powerful tools for the interpretation of both theoretical and experimental data; and therefore, the number of ab initio and experimental studies continues to grow [6–11]. From the perspective of inorganic perovskite ABO_3-type materials, the prototype $PbTiO_3$ ferroelectric oxide and their Pb-based oxide solid solutions provide most of the technologically useful ferroelectric materials, which are dominant candidates for electro-active material applications [12,13]. Their corresponding properties, such as ferroelectric, piezoelectric, dielectric, optical, and electronic states are strongly influenced by the amount of substitution in the A (twelve-fold coordination) and/or B (six-fold coordination) sites [14–16].

In particular, the density functional theory (DFT) approach offers an opportunity for a rational design of new materials with improved properties, even before they are observed

* Corresponding author.
E-mail address: fenelon@fc.unesp.br (F.M. Pontes).

http://dx.doi.org/10.1016/j.jallcom.2017.01.250
0925-8388/

experimentally. Brehm et al. [17] reported physical and electronic properties of hypothetical $PbTiO_3$-based oxysulfides, $PbTiO_{3-x}S_x$ using first-principles calculations. Theoretical analysis indicates that this compound should be considered a solar bulk photovoltaic material candidate [17]. First-principles calculations conducted by Cohen [18] revealed that the strong interaction between the Ti 3d orbitals and O 2p orbitals, or in other words covalent bonding, is crucial for large polarization of lead titanate, $PbTiO_3$. In addition, the fundamental characteristics of the hybridization between Pb 6s, 6p, and O 2p orbitals (also responsible for the large tetragonality of lead titanate, $PbTiO_3$) has been demonstrated by first principles calculations using full potential linearized augmented plane wave (FLAPW) method with the local density approximation (LDA) [19]. Because of $PbTiO_3$ structure to be capable of accommodating a large number of cation substitutions, a meaningful development of new semiconducting ferroelectric complex perovskite oxides is opened up.

Previous studies [20] on structural and electronic behaviors of two possible (001) surface terminations of cubic $PbTiO_3$ using first-principles calculations based on density functional theory (DFT) showed a partial covalent character of the Ti—O bonds, especially in the TiO_2-terminated surface layer, and of the (110) plane, whereas the Pb—O bonds showed a very low covalent character. Recently, Shimada et al. [21] investigated whether or not ferroelectricity can exist in $PbTiO_3$ nanotubes using first-principles density functional theory calculations. Paris et al. [22] also reported experimental and theoretical studies on the $(Pb_{1-x}Sm_x)TiO_3$ system. Recently, first-principles studies on $PbTi_{1-x}Ni_xO_{3-x}$ solid solutions have indicated the important role of B-site Ni and Ti cation ordering [23]. A combined experimental and theoretical study has shown that $PbZr_{0.30}Ti_{0.70}O_3$ doped with tungsten thin films deposited on $LaNiO_3$ bottom electrodes by pulsed laser deposition are less susceptible to fatigue than undoped-PZT films [24]. Furthermore, theoretical investigations have shown that the fatigue phenomenon in the PZT system is associated with a small overlap of π bonds between Ti 3d and O 2p states. A recent publication by Lee et al. [25] reported a combination of theoretical and electrical studies on the effect of nanometer-thick in $SrTiO_3$ films. They presented evidence of room temperature ferroelectricity in thinning $SrTiO_3$ films. Seidel et al. conducted a theoretical and experimental study using a combination of conductive atomic force microscopy, transmission electron microscopy, and first-principles density functional calculations for $BiFeO_3$ [26].

The purpose of the present work is to perform a combination of nanoscale piezoresponse force microscopy experimental analysis and first-principles calculations based on density functional theory (DFT) to study the ferroelectric and electronic properties of the $Pb(Ca,Ba)TiO_3$, $Pb(Sr,Ba)TiO_3$, and $Pb(Sr,Ca)TiO_3$ complex perovskite solid solutions, classified as $A(A'A'')BO_3$ ($A = Pb$, $A' = Ca$ and Sr and $A'' = Ba$ and Sr).

2. Experimental procedures

The synthesis of $PbTiO_3$-based complex perovskite oxides co-substituted at the A-site with isovalent cation pairs (Ca^{2+}/Ba^{2+}), (Sr^{2+}/Ba^{2+}), and (Sr^{2+}/Ca^{2+}) was based on the chemical solution deposition (CSD) method commonly known as the polymeric precursor route. Details of the preparation method can be found in the literature [27,28]. Ceramic and thin film samples with nominal chemical compositions of $Pb_{0.60}(Ca_{0.20},Ba_{0.20})TiO_3$, $Pb_{0.60}(Sr_{0.20},Ba_{0.20})TiO_3$, and $Pb_{0.60}(Sr_{0.20},Ca_{0.20})TiO_3$, hereafter referred to as PCBT-60, PSBT-60, and PSCT-60, respectively, were prepared. The precursor solution was deposited onto a $Pt/Ti/SiO_2/Si$ commercial substrate by spin coating at 6000 rpm for 20 s using a spin coater (KW—4B, Chemat Technology) via a syringe filter to avoid particulate contaminations.

After spin coating, the films were preheated to 200 °C for 10 min on a hot plate to remove residual water. Then, the films were annealed using a stepwise/successive growth and crystallization engineering method at 400 °C for 4 h and 700 °C for 2 h in air to remove residual organic components at a heating rate of 5 $°Cmin^{-1}$, respectively. The film thickness was adjusted by repeating the deposition and pyrolysis/growth/crystallization cycle. The thicknesses of PCBT-60, PSBT-60 and PSCT-60 films were adjusted to 300, 280, and 310 nm, respectively.

The phase structures of the samples were identified using a Rigaku MiniFlex600 X-ray diffractometer ($CuK_\alpha = 1.54056$ Å radiation). In order to more accurately determine the crystallographic structure, the Rietveld refinement technique was performed using the General Structure Analysis System (GSAS) software.

The surface morphology, polarization patterns of the ferroelectric domain structures, and the local hysteresis loops of ferroelectric films were investigated at the nanoscale level using a commercial atomic force microscope (AFM) (MultiMode Nanoscope V, Bruker) modified to function as a piezoresponse force microscope (PFM). The system was equipped with a lock-in amplifier (SR850, Stanford) and a function generator (33220A, Agilent). During all PFM measurements, the conductive probe was electrically grounded and an external voltage was applied to the bottom Pt electrode operated at a driving amplitude of 1 V (rms).

3. Computational methods and model systems

To further study the effect of AO_{12}-site double chemical substitution by either (Ca^{2+}/Ba^{2+}), (Sr^{2+}/Ba^{2+}), or (Sr^{2+}/Ca^{2+}) isovalent cation pairs of the $PbTiO_3$ perovskite lattice, first-principles calculations within the framework of density functional theory (DFT) were used. Using this method, energy variations of the different structure symmetries can be evaluated and the corresponding ferroelectric, optical, and electronic properties can be obtained with precision. Calculations were carried out with the CRYSTAL06 [29] package using the gradient-corrected correlation functional by Lee, Yang, and Parr, combined with the Becke3 exchange functional, B3LYP [30,31].

The Pb, Ti, O, Ba, Sr and Ca atomic centres were described by all electron basis sets [DB]-31G, 86-411(d31), 6-31G*, 311(1d)G, 311(3d)G, and 86-511d(21)G, respectively. Here [DB] denotes the Durand—Barthelat non-relativistic large effective core potential, and all basis sets can be found at the CRYSTAL home page. In the theoretical calculations, $1 \times 1 \times 5$ supercells for all systems were built, as shown in Fig. 1. To initiate structural modeling, tetragonal symmetric $PbTiO_3$ (space group *P*4*mm*), PCBT-60, PSBT-60, and PSCT-60 systems were constructed based on the Rietveld refinement analysis using lattice parameters and atomic positions displayed in Table 1.

4. Results and discussions

Fig. 2(i) shows the XRD patterns of the PCBT-60, PSBT-60, and PSCT-60 thin films on platinum-coated silicon substrates. All the thin films are found to possess polycrystalline features with pure perovskite phases within the detection limits of XRD. In addition, the diffraction peaks for all the thin films are indexed to the tetragonal phase by considering the obvious splitting of the (101)/(110) peaks. In order to clarify the structure evolution, Fig. 2(ii) shows in detail that the (101) and (110) peaks clearly overlap and shift towards higher scattering angles for the PSCT-60 thin film compared with the PCBT-60 and PSBT-60 thin films, indicating both a decrease in the *d* spacing and tetragonality (*c*/*a* ratio).

To further confirm the structural evolution, the crystal

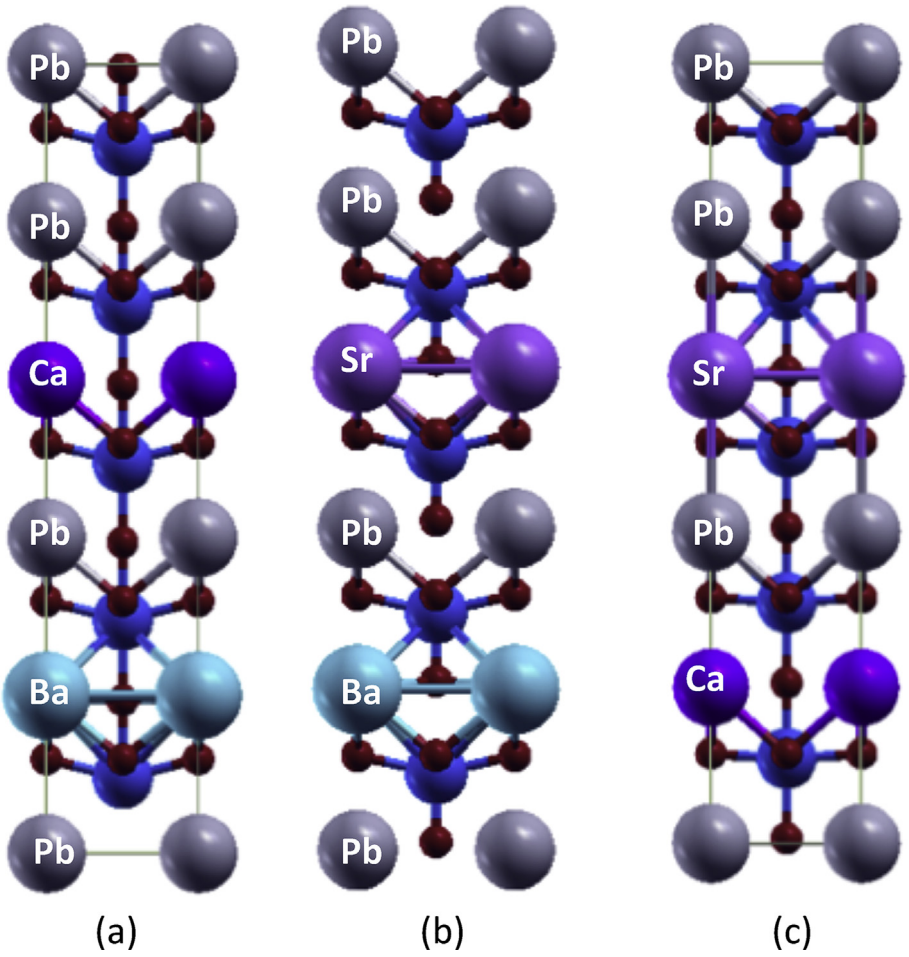

Fig. 1. Schematic 1 × 1 × 5 supercells model construction for (a) PCBT-60, (b) PSBT-60 and (c) PSCT-60 structure. Red atoms = oxygen. Blue atoms = titanium. (For interpretation of the references to colour in this figure legend, the reader is referred to the web version of this article.)

Table 1
Lattice parameters and atomic positions obtained of Rietveld Refinement of the powders X-ray diffraction data collected to PCBT-60, PSBT-60 and PSCT-60 sample and reliability factors (χ^2, R_p, R_{wp}, R_{Bragg} in %).

Cell Parameters	Samples		
	PCBT-60	PSBT-60	PSCT-60
a (Å)	3.919	3.931	3.905
b (Å)	3.919	3.931	3.905
c (Å)	4.021	4.006	3.966
V (Å^3)	61.77	61.92	60.48
c/a	1.026	1.019	1.015
z(Ti1)	0.47884	0.47888	0.54514
z(O2)	−0.0300	0.05078	0.02993
xy plane, *z*(O4)	0.5976	0.58731	0.57561
χ^2	3.75	3.29	3.25
R_p	4.51	4.18	3.67
R_{wp}	5.94	5.24	4.55
R_{Bragg}	1.92	1.03	1.89

structures of PCBT-60, PSBT-60, and PSCT-60 samples were refined by the Rietveld method using XRD powder data collected at room temperature. Rietveld refinements were successfully performed on the basis of the tetragonal *P4mm* perovskite structure shown in Fig. 3. The most important structural parameters at room temperature and reliability factors (χ^2, R_p, R_{wp}, R_{Bragg}) after refinement are listed in Table 1. A view of the refined room temperature crystal structure is shown in Fig. 4. In addition, careful inspection indicates that the distortion of the TiO_6 clusters is more intense in PCBT-60 and PSBT-60 when compared to PSCT-60, indicating that there is only a modest distortion of the TiO_6 cluster units (see angles and bonding length parameters in Table 2). In addition, the results this refinement clearly shows a symmetry reduction from pseudocubic to tetragonal one. These results reflect a small dipole moment, which will contribute to weak ferroelectric activity in PSCT-60 thin films. These outcomes will be confirmed by nanoscale electrical measurements and first-principles calculations based on density functional theory as follows.

In order to conduct an electrical properties approach, the powerful piezoresponse force microscopy technique was utilized to reveal both the localized piezoelectric and ferroelectric domain switching responses. The out-of-plane (OP) piezoresponse images of PCBT-60, PSBT-60, and PSCT-60 thin films on platinum coated silicon substrates were obtained within an area of 5 μm × 5 μm, as shown in Fig. 5. For all films, the OP piezoresponse images exhibit distinct colors, which can be interpreted as domain structures with random orientations [32,33]. In addition, some regions manifest considerable contrasts containing either an upward (bright contrast) or a downward (dark contrast) polarization component. Interestingly, one important aspect of the OP PFM images is the piezosignal response of all the three films. For PCBT-60 and PSBT-60 thin films, the OP PFM images show an area with high piezoelectric response, whereas the PSCT-60 films reveal a low piezoelectric response. The discrepancy in piezoelectric response symbolizes

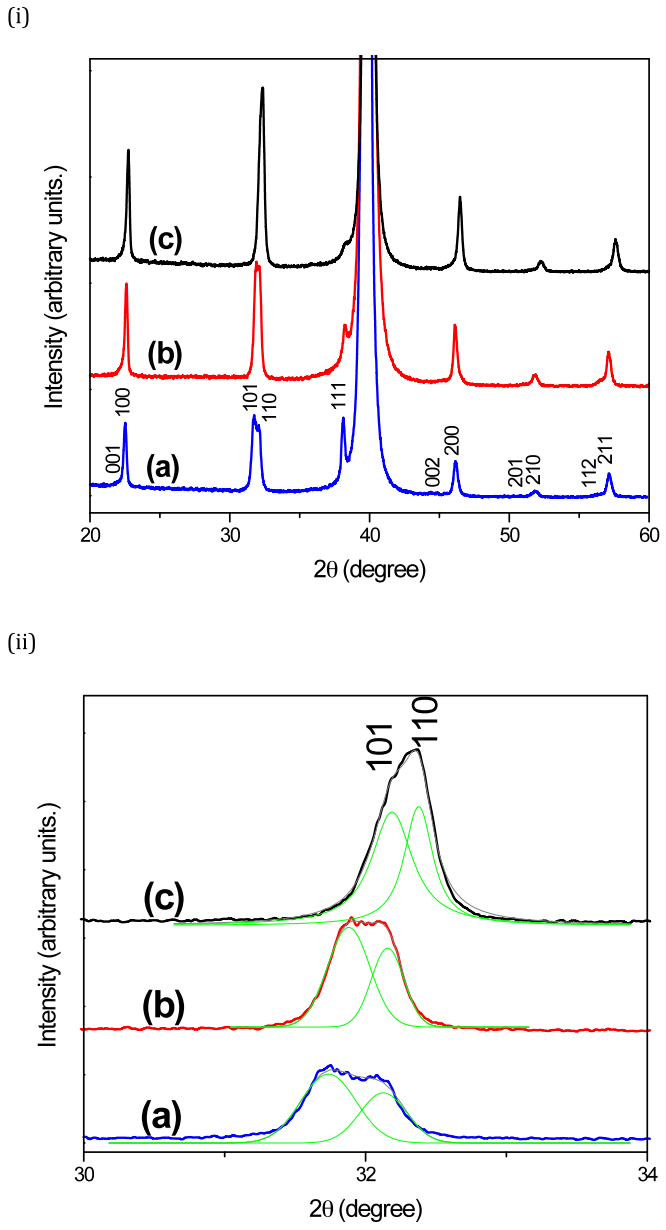

Fig. 2. (i) XRD patterns of (a) PCBT-60, (b) PSBT-60, and (c) PSCT-60 thin films deposited on Pt/Ti/SiO_2/Si substrates. (ii) Details show overlapping of the peaks 101/110.

different polarization behaviors among these thin films. Therefore, the low piezoresponse signal for the case of PSCT-60 relative to the PCBT-60 and PSBT-60 films should be ascribed to the reduced polarization (electric dipole), or in other words, weak ferroelectricity. This characteristic can be interpreted as the dominant role of the TiO_6 sublattice distortion levels in these films, which is consistent with crystal structure results determined by XRD Rietveld refinement.

It is well known that the ferroelectric domains can be locally switched by applying a bias. Therefore, the ferroelectric polarization switching behavior of the different thin films was investigated. Fig. 6 exhibits the results of the application of a DC voltage of −20 V to +20 V to the conductive tip of the PFM on selected regions of the thin films.

It can be clearly seen that the piezoresponse signals of the scanned regions (within solid white lines in the PFM images) dramatically change after the poling process: The region previously positively poled (bright contrast) was effectively switched and the grains became negatively poled (dark contrast), establishing a nanoscale domain switching response; this feature undoubtedly/presumably emphasizes the ferroelectric nature of all the three films.

In order to obtain insight on the ferroelectric polarization switching behavior of all films, the piezohysteresis loops on selected individual ferroelectric grains were also recorded. Fig. 7 shows the typical piezohysteresis loops of all three films. As a confirmation, these piezohysteresis loops reveal the reverse ferroelectric polarization for all films. However, as a remark, it is noticeable that the PCBT-60 and PSBT-60 thin films show well saturated and widely open piezohysteresis loops, suggesting a clear enhancement in the electric polarization switching response, commonly attributed to a large Ti off-center displacement at the TiO_6 octahedral units (see Fig. 6 (c) and (f)). In contrast, for the PSCT-60 thin films, the polarization switching portion decayed significantly, producing slimmer piezohysteresis loops and suggesting that there is a small Ti off-center displacement, and therefore, weakening the short- and long-range electric dipole displacement (polarization) of the Ti atoms inside the oxygen octahedral cage (see Fig. 6 (i)).

Finally, to better understand the effects of Sr, Ca, and Ba atoms on the ferroelectric behavior of the PCBT-60, PSBT-60, and PSCT-60 thin films recorded at the nanoscale, an evaluation from the electronic structure perspective by first-principles calculations has been performed to provide a qualitative explanation. The density functional theory (DFT) results have shown that the ferroelectric and tetragonal phase instabilities of these compounds originate from a delicate interplay between the nature of chemical bonding, bonding, anti-bonding, and non-bonding orbital state densities and hybridization strengths.

Therefore, as a starting point for the theoretical calculations, the electronic structure of $PbTiO_3$, known as the prototype of classical ferroelectrics, was firstly determined.

Fig. 8 displays the partial and total density of states (DOS) of tetragonal $PbTiO_3$ for the Ti, O, and Pb atoms. The contribution of O atoms is mainly found in the valence band (VB) starting from energy levels of around −8.0 eV to −3.5 eV, together with a small contribution from the Ti d and Pb s states; while for the Ti atoms, the contribution is mainly located in the conduction band (CB) from about −0.5–4.0 eV, together with a small contribution of the O p and Pb s states. In addition, for the Pb atoms, their partial DOS contribution in the valence and conduction bands is much smaller than those of the O and Ti orbitals, respectively. In addition, examining the $PbTiO_3$ partial DOS in detail, the top of the valence band contains stronger admixtures of Pb s and O p orbitals in comparison to PCBT-60, PSBT-60, and PSCT-60 partial DOS; this represents a stronger Pb–O covalency, which in turn stabilizes the larger ferroelectric tetragonal phase in the $PbTiO_3$ prototype. This observation is consistent with many simulation results reported in the literature [34,35]. From the calculated DOS for PCBT-60, PSBT-60, and PSCT-60 electronic structures, it can be observed that for all three compounds the VB is predominantly composed of O p states, whereas Ti d states contribute predominantly to the CB, as seen Fig. 8. It should also be noted that the partial DOS show negligible amounts of Ca (Sr and Ba) atom electronic density of states, indicating poor interaction between the O p and Ca (Sr and Ba) s states and confirming that the A-O (A = Ca, Sr and Ba) bond is of ionic nature. Therefore, the ionic nature of the A-O bond has been observed as one of the key factors of the moderate ferroelectric activity of PCBT-60, PSBT-60, and PSCT-60 as compared to $PbTiO_3$ [36]. Choudhury et al. [36] reported that the covalent nature of the Pb–O bond is responsible for the strong ferroelectric tetragonal

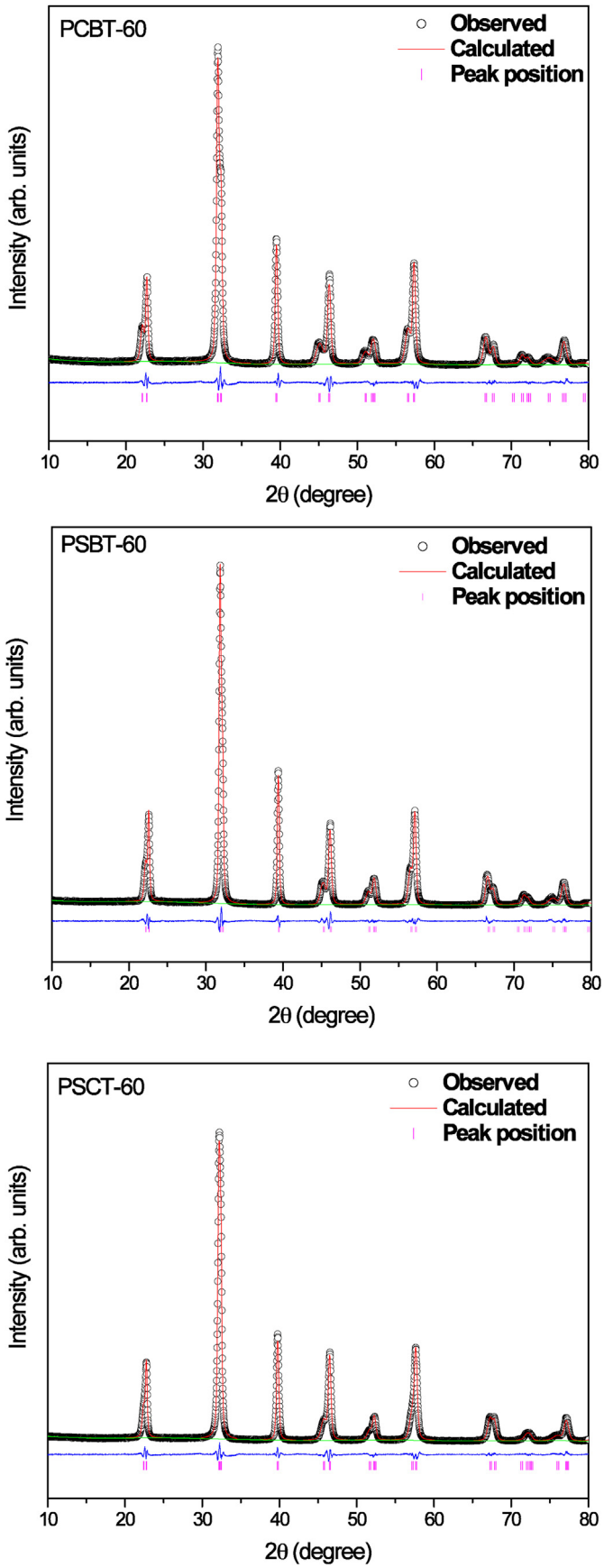

Fig. 3. Rietveld refinement for PCBT-60, PSBT-60, and PSCT-60 powder samples where the "o" symbols represent the measured XRD reflections and the solid red lines are the Rietveld refined results. The short vertical solid lines are guides for the corresponding Bragg positions. (For interpretation of the references to colour in this figure legend, the reader is referred to the web version of this article.)

phase in $PbTiO_3$ using first-principles calculations; this is in contrast to the ionic nature of Ba—O bonds, which is important for the stabilization of the rhombohedral phase of $BaTiO_3$. Recently, Luo et al. [9] demonstrated, also using first-principles calculations, that the strong hybridization between Ti 3d and O 2p orbitals is responsible for the ferroelectricity of $BaTiO_3/CaTiO_3/SrTiO_3$ ferroelectric superlattices, although the Ba—O, Ca—O, and Sr—O bonds are found to be of ionic nature.

In addition, the O p electronic density states (VB) in the PCBT-60, PSBT-60, and PSCT-60 compounds obviously shift to a higher energy side, indicating a gap lowering. It should also be noted that the valence and conduction bands of PCBT-60, PSBT-60, and PSCT-60 are extremely narrow due to the smaller extension hybridization between the Pb and O atoms. As a result, there is a tendency of weak covalency in Pb—O bonds. This scenario demonstrates a general trend towards a reduction of tetragonality and ferroelectricity in PCBT-60, PSBT-60, and PSCT-60 relative to the $PbTiO_3$ prototype. This is supported by PFM-based experimental results conducted in the nanometer range.

Therefore, to further analyze the electronic origin of the reduction of the ferroelectric order in PCBT-60, PSBT-60, and PSCT-60 thin films, the superposition of the electronic density of states of the atomic orbitals of the Ti and O atoms (Fig. 9) was separately. The main DOS features can be summarized as follows. In the case of $PbTiO_3$ (reference), the broad O 2p band appears in the VB, while the broad Ti 3d band is mainly found in the CB. Furthermore, the valence and conduction band regions clearly illustrate the presence of rather strong hybridization between the Ti 3d and O 2p states (hybrid orbitals – red areas), mainly consisting of bonding and antibonding orbitals, while the lower part of the CB is exclusively formed by participation (availability) of Ti $3d_{yz}$ non-bonding orbitals. All these contributions reflect the presence of a higher polar structural distortion, which is responsible for large ferroelectricity in $PbTiO_3$. As already mentioned, for PCBT-60, PSBT-60, and PSCT-60 compounds, the presence of an ionic character (Ca—O, Sr—O, and Ba—O bonding) also indirectly leads to a small hybridization extension between Ti 3d and O 2p states (Fig. 9), which exhibits a relatively small polar structural distortion. However, the most striking feature when comparing the electronic structures of $PbTiO_3$, PCBT-60, PSBT-60, and PSCT-60 perovskite oxides by DFT calculations can be found in the minimum of the CB region as shown in Fig. 9. Specifically, the contribution of Ti $3d_{yz}$, Ti $3d_{xz}$, Ti $3d_{xy}$, and Ti $3d_{xy}$, d_{yz} non-bonding orbitals decreases monotonically in the following order: $PbTiO_3$, PCBT-60, PSBT-60, and PSCT-60, respectively. As an assumption, it was expect that the participation of non-bonding orbitals (responsible for π Ti—O bonding, dπ -pπ, respectively) play a key role in the Ti—O bond displacements inside the TiO_6 octahedron (breathing oxygen cage distortion, see Fig. 6 (c, f, and i). Then, the greater the presence of the non-bonding electronic density of states is, the greater will the Ti—O bond polar distortion (more intense breathing oxygen cage distortion) become, leading to a large charge displacement (high distortion, more separation of positive and negative charges, polar $[TiO_6]$ clusters); therefore, a stronger local electric polarization effect (ferroelectric activity) will be observed. In general, the very little contribution from Ti $3d_{xy}$, d_{yz} non-bonding orbitals is a vital factor for the reduced ferroelectricity in PSCT-60 thin films relative to PCBT-60 and PSBT-60 thin films; this observation is fully supported by the PFM-based experimental results at the nanoscale. This clearly demonstrates that the dissimilar behavior of PCBT-60, PSBT-60, and

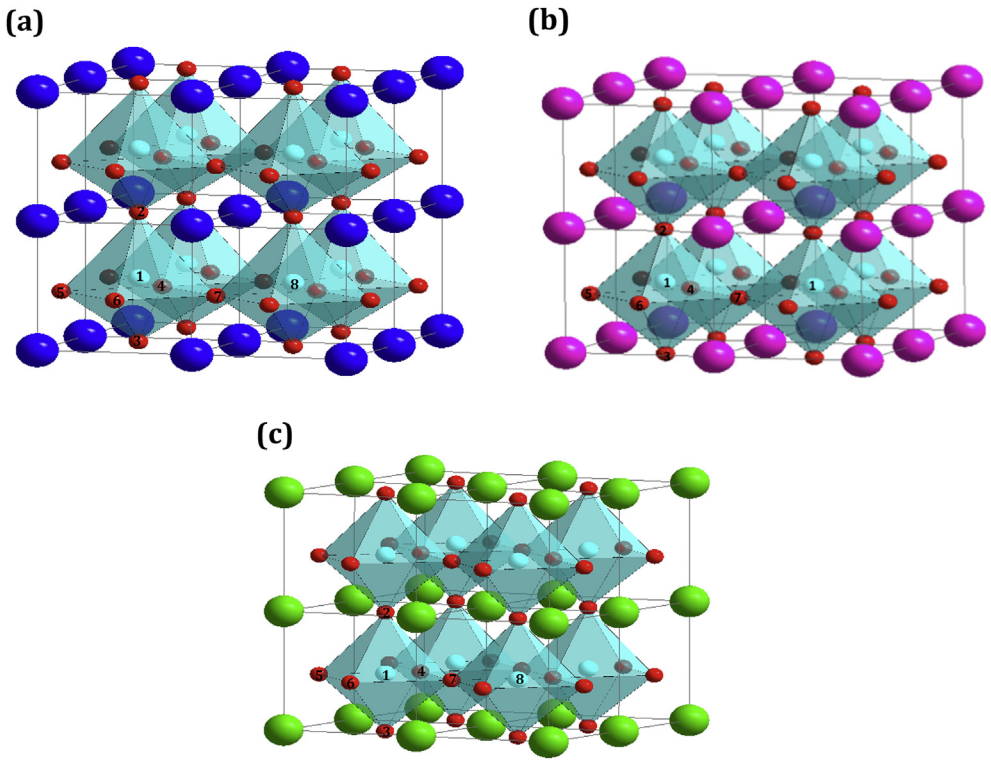

Fig. 4. Crystal structure of PCBT-60 (a), PSBT-60 (b) and PSCT-60 (c) samples obtained from the Rietveld analysis. Green atoms = strontium, calcium or lead. Cyan atoms = titanium. Red atoms = oxygen. Pink atoms = strontium, barium or lead. Dark blue atoms = lead, calcium or barium. (For interpretation of the references to colour in this figure legend, the reader is referred to the web version of this article.)

Table 2
Bond length and bond angles calculated using the parameters obtained from Rietveld analysis for PCBT-60, PSBT-60 and PSCT-60 samples.

Parameters	Samples		
	PCBT-60	PSBT-60	PSCT-60
Bond Length (Å)			
Ti(1)–O(2)	2.0460	1.7150	2.0433
Ti(1)–O(3)	1.9749	2.2912	1.9227
Ti(1)–O(4,5,6,7)	2.0171	2.0132	1.9562
Bond Angles (degree)			
Ti(1)–O(7)–Ti(8)	152.590	155.078	172.917
O(2)–Ti(1)–O(5)	103.705	102.461	93.541
O(4)–Ti(1)–O(5)	86.782	87.321	89.781
O(5)–Ti(1)–O(3)	76.295	77.539	86.459

PSCT-60 complex perovskite films is almost entirely due to the change in stability of the Ti—O non-bonding orbitals bonds.

Additional information about the electric dipole (polarization) nature of the compounds can be obtained from the Mulliken charges analysis. Therefore, the well-known clusters structural model [11] was adopted to provide detailed information to further illustrate the particular manifestation of ferroelectric polarization in PCBT-60, PSBT-60, and PSCT-60 complex perovskite solid solutions. Considering that the introduction of different atoms into the $PbTiO_3$ perovskite lattice can lead to the formation of a structural order/disorder both in the network modifier site (AO_{12}, where A = Pb, Ca, Sr, and Ba) and in the network former (BO_6, where B = Ti), it is possible to define this structural order/disorder by different clusters, for example, $[TiO_6]/[TiO_5.VO^{\bullet}]$, $[PbO_{12}]/[PbO_{11}.VO^{\bullet}]$, and $[CaO_{12}]/[CaO_{11}.VO^{\bullet}]$, etc. The schematic representation of the structural disorder of both the network modifier and former is displayed in Fig. 10. According to some authors [11,37–40], these species (clusters) play a central role in the formation of electric dipoles (polarization), i.e., creating electron-hole pairs (e'-$h^{\bullet}$) in the $A(A'A'')BO_3$ perovskite lattice.

In the case of the network modifiers, the equations that represents the disorder clusters model in the $A(A'A'')BO_3$ perovskite lattice are

$$[PbO12]^{x} + [CaO11.VO^{x}] \rightarrow [PbO12]^{'} + [CaO11.\ VO^{\bullet}], \quad (1)$$

$$[PbO12]^{x} + [BaO11.VO^{x}] \rightarrow [PbO12]^{'} + [BaO11.\ VO^{\bullet}], \quad (2)$$

$$[PbO12]^{x} + [SrO11.\ VO^{x}] \rightarrow [PbO12]^{'} + [SrO11.\ VO^{\bullet}], \quad (3)$$

and for the network former the equation is:

$$[TiO6]^{x} + [TiO5.VO^{x}] \rightarrow [TiO6]^{'} + [TiO5.\ VO^{\bullet}], \quad (4)$$

where $[TiO_6]'$ and $[PbO_{12}]'$ are donor-type clusters (electrons) and $[TiO_5.V_O^{\bullet}]$, $[CaO_{11}.V_O^{\bullet}]$, $[BaO_{11}.V_O^{\bullet}]$, and $[SrO_{11}.V_O^{\bullet}]$ are considered acceptor-type clusters (holes).

Table 3 lists the Mulliken charges variations for each individual cluster of PCBT-60, PSBT-60, and PSCT-60 complex perovskites. As can be seen, it is demonstrated that the Mulliken negative charges of $[TiO_6]'$ and $[PbO_{12}]'$ clusters simultaneously decrease as the covalent bonds weaken and the ionic bonds strengthen in the perovskite lattice. Furthermore, it can be assumed that the charge redistribution or charge transference between clusters may lead to different electric dipole responses (polarization) for PCBT-60, PSBT-60, and PSCT-60 complex perovskites. Moreover, our analysis shows that the Mulliken charges in $[BaO_{11}.V_O^{\bullet}]$ clusters are higher than those of the $[SrO_{11}.V_O^{\bullet}]$ and $[CaO_{11}.V_O^{\bullet}]$ clusters, independently

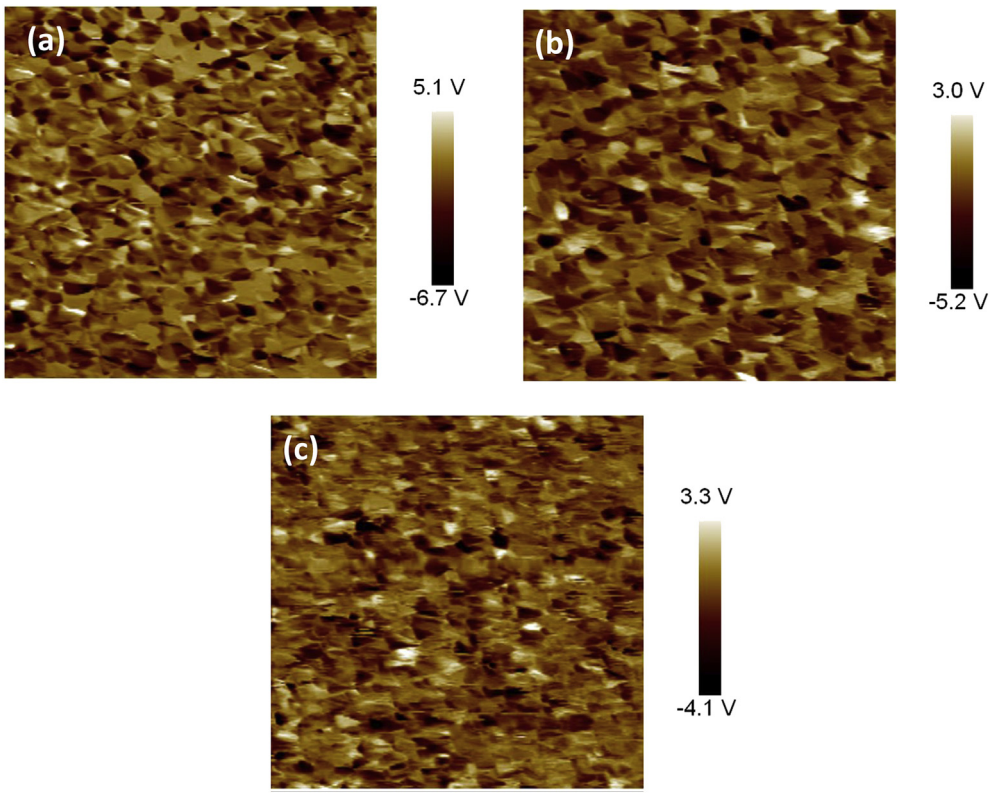

Fig. 5. Out-of-plane PFM images of (a) PCBT-60, (b) PSBT-60, and PSCT-60 thin films deposited on $Si/SiO_2/Ti/Pt$ substrates. The scan size is 5 μm × 5 μm.

from the perovskite compounds. These results also suggest that the $[BaO_{11}.V_O^{\bullet}]$ clusters play a dominant role for the stability of the ferroelectricity in perovskite compounds, leading to a high net global electric polarization.

In this regard, it is interesting to compare the charge recombination between donor and acceptor local clusters, which in turn define the appearance of the local electric dipole (polarization) in the perovskite lattice (Fig. 10).

To unravel the polarization behavior, the donor and acceptor cluster recombination was adopted for each network modifier and former, and then combined the Mulliken charge values (Table 3). For example, the net charge changes between donor and acceptor clusters for PCBT-60 occurred, as shown in equations (1), (2) and (4), for PSBT-60, as shown in equations (2)–(4), and for PSCT-60, as shown in equations (1), (3) and (4). The Mulliken charge analysis for each cluster group gives the following net effective charges:

For PCBT-60:

Donors clusters + aceptors clusters → clusters pairs charge

$$[PbO_{12}]^{'} + [BaO_{11}.VO^{\bullet}] \rightarrow -4605 \quad (5)$$

$$[PbO_{12}]^{'} + [CaO_{11}.V_O^{\bullet}] \rightarrow -4542 \quad (6)$$

$$[TiO_6]^{'} + [TiO_5.V_O^{\bullet}] \rightarrow -3082 \quad (7)$$

For PSBT:

$$[PbO_{12}]^{'} + [BaO_{11}.V_O^{\bullet}] \rightarrow -4456 \quad (8)$$

$$[PbO_{12}]^{'} + [SrO_{11}.V_O^{\bullet}] \rightarrow -4402 \quad (9)$$

$$[TiO_6]^{'} + [TiO_5.V_O^{\bullet}] \rightarrow -2861 \quad (10)$$

For PSCT-60:

$$[PbO_{12}]^{'} + [CaO_{11}.V_O^{\bullet}] \rightarrow -4283 \quad (11)$$

$$[PbO_{12}]^{'} + [SrO_{11}.V_O^{\bullet}] \rightarrow -4218 \quad (12)$$

$$[TiO_6]^{'} + [TiO_5.V_O^{\bullet}] \rightarrow -2596 \quad (13)$$

As a general observation, the above analysis shows that increasing the net donor and acceptor cluster charge recombination also increases the electric dipole strength (polarized cluster pairs). On the other hand, low values of net donor and acceptor cluster charge recombination usually indicate weak electric dipoles. In summary, equations (5)–(7) suggest that there is a strong polarization in the PCBT-60 complex perovskite structure as compared with that in PSBT-60 and PSCT-60 structures. Again, our theoretical results show excellent cohesion with the PFM-based experimental results at the nanoscale.

As already discussed, it was found that a strong correlation exists between the Mulliken cluster charges and experimental polarization responses of PCBT-60, PSBT-60, and PSCT-60 thin films. This means that first-principles calculations of local electronic structures may serve as excellent estimators of materials properties (for example, ferroelectric polarization) of unexplored ABO_3-based complex perovskites solid solutions.

To further study the electronic properties of $PbTiO_3$, PCBT-60, PSBT-60, and PSCT-60 systems, the calculated band structures were further analyzed and are shown in Fig. 11. In the tetragonal $PbTiO_3$ band structure, the smallest band gap appears as indirect band gap of 3.31 eV localized between the X and Γ points. Similar

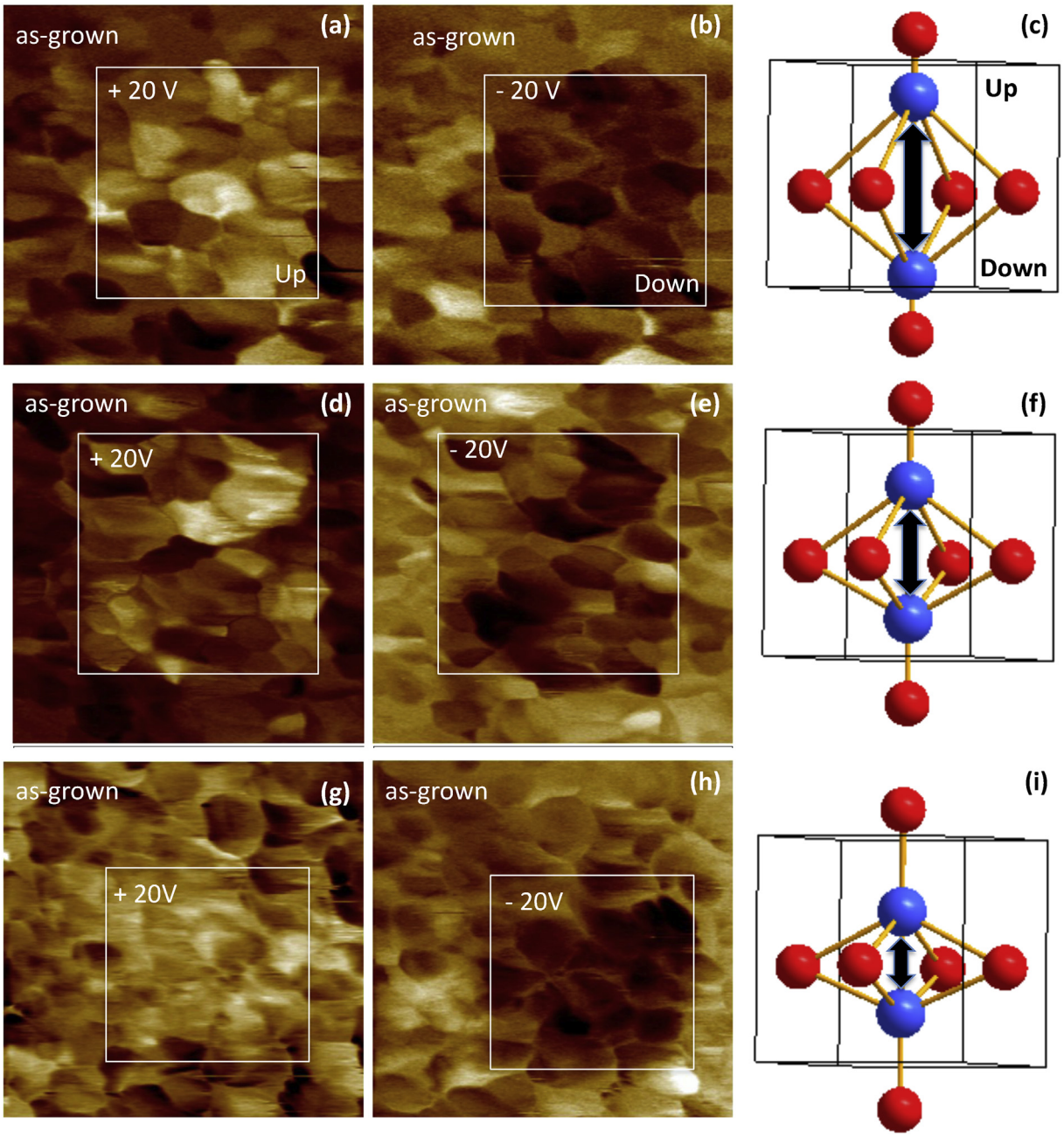

Fig. 6. PFM images of thin films PCBT-60 (a, b), PSBT-60 (d, e), and PSCT-60 (g, h) recorder after the application of +20 V and −20 V, where the solid white lines indicate the switched region. Schematic illustration of the Ti off-center displacement, breathing oxygen cage, for PCBT-60 (c), PSBT-60 (f), and PSCT-60 (i), respectively.

results were reported by Lazaro et al. [20] studying structural and electronic properties of $PbTiO_3$ slabs. The band structures of the PCBT-60, PSBT-60, and PSCT-60 complex oxides relative to $PbTiO_3$ show a narrowing of the band gap energy. In the case of the PCBT-60 an indirect gap of 2.91 eV located between the R to Γ points was observed, while PSBT-60 and PSCT-60 exhibit an indirect gap of 3.25 eV and 3.03 eV located between the A to Γ and X to Γ points, respectively.

5. Conclusions

A combined experimental and theoretical study has been conducted to understand the ferroelectric and electronic properties of $Pb(Ca,Ba)TiO_3$, $Pb(Sr,Ba)TiO_3$, and $Pb(Sr,Ca)TiO_3$ complex perovskite solid solutions. The main conclusions can be summarized as follows: (i) The structural analysis undertaken using Rietveld refinement revealed that the simultaneous incorporation of isovalent Ca–Ba, Sr–Ba, and Sr–Ca chemical species at the A-site of the $PbTiO_3$ perovskite oxide decreases the tetragonality and significantly reduces the octahedron distortion. (ii) From the local piezohysteresis experiments, it was observed that the ferroelectric polarization switching in response to an applied electric field was very different between three thin films. Well-defined and saturated local piezohysteresis loops on a single grain for the $Pb(Ca,Ba)TiO_3$ and $Pb(Sr,Ba)TiO_3$ thin films were observed due to high tetragonal distortion (large Ti off-center displacement), while slim

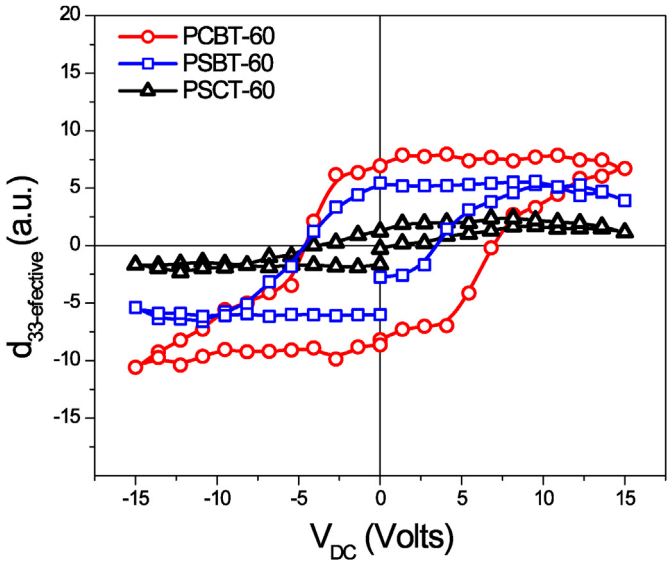

Fig. 7. Local piezoresponse hysteresis loops measured by PFM for PCBT-60, PSBT-60 and PSCT-60 thin films.

piezohysteresis loops were observed for the $Pb(Sr,Ca)TiO_3$ thin films due to low tetragonal distortion (small Ti off-center displacement). (iii) Analysis of the electronic density of states (DOS) revealed that although the Ca, Sr, and Ba atomic orbitals do not contribute directly to the partial DOS, O, Ti, and Pb atomic orbitals are influenced by the Ca, Sr, and Ba substitution. Our results showed that adding Ca, Sr, and Ba atoms to the $PbTiO_3$ system decreases the overlapping between O 2p and Ti 3d orbitals responsible for high tetragonal polar distortion. (iv) It was demonstrated that the weak hybridization between Ti 3d and O 2p states and high contribution of ionic Ca–O and Sr–O bonding are the main forces behind the dramatic Ti 3d non-bonding orbital participation weakening. This phenomenon is responsible for Ti atoms displacements inside the octahedral oxygen cage, and hence, destabilizes the local electric dipole interactions vital for the ferroelectric tetragonal structure of the $PbTiO_3$ prototype. (v) The Mulliken charge values between clusters of disordered models show that there is a strong polarization between clusters in $Pb(Ca,Ba)TiO_3$ complex perovskite oxides as compared to $Pb(Sr,Ba)TiO_3$ and $Pb(Sr,Ca)TiO_3$ complex perovskite oxides. (vi) Our calculated band structures show indirect band gaps with values of about 3.31 eV between X to Γ, 2.91 eV located between R to Γ, 3.25 eV

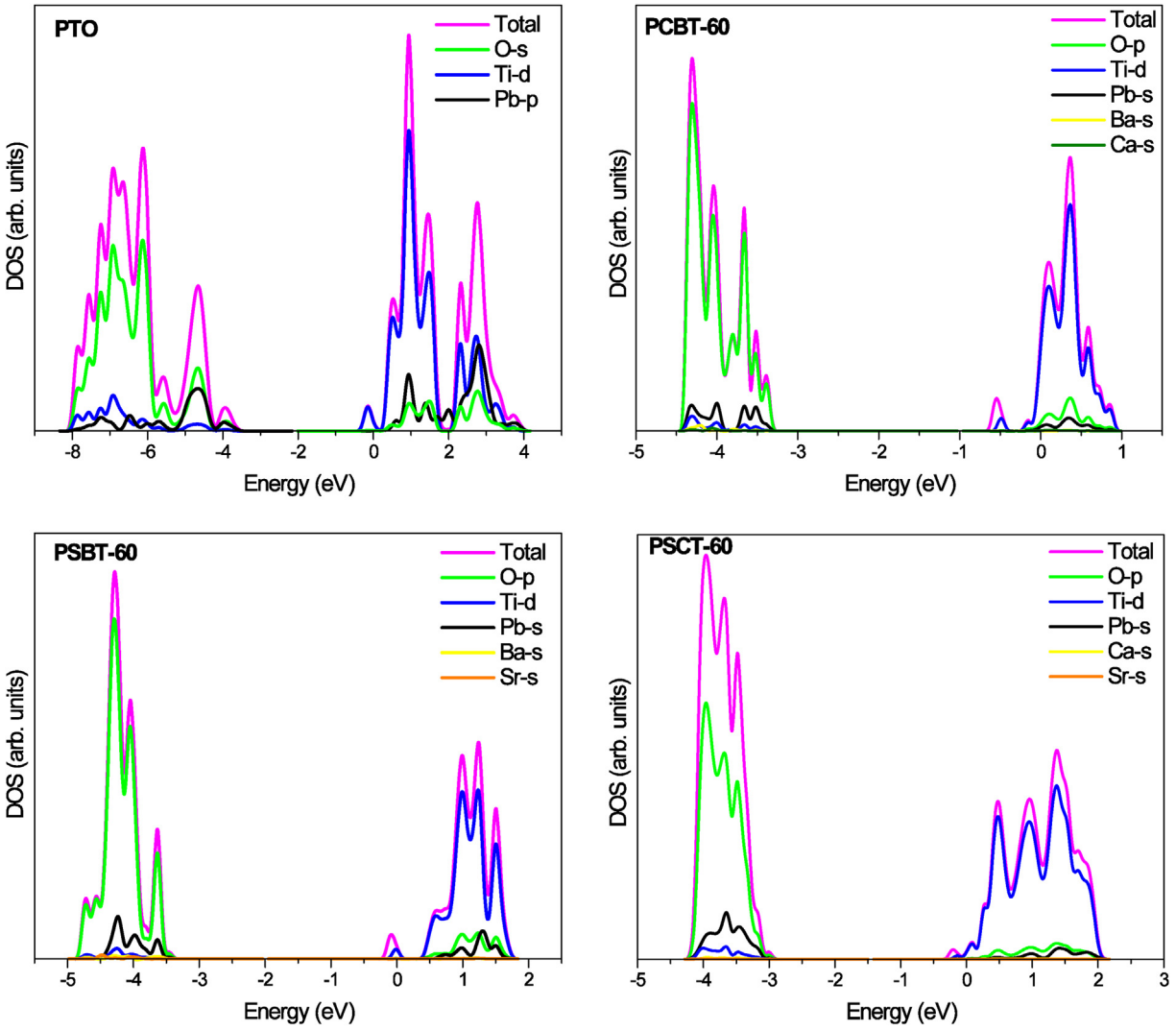

Fig. 8. Total and partially calculated density of states projected for the Pb, O, Ti, Ca, Sr, and Ba atomic orbitals in the *P4mm* phase of PTO, PCBT-60, PSBT-60, and PSCT-60 perovskite.

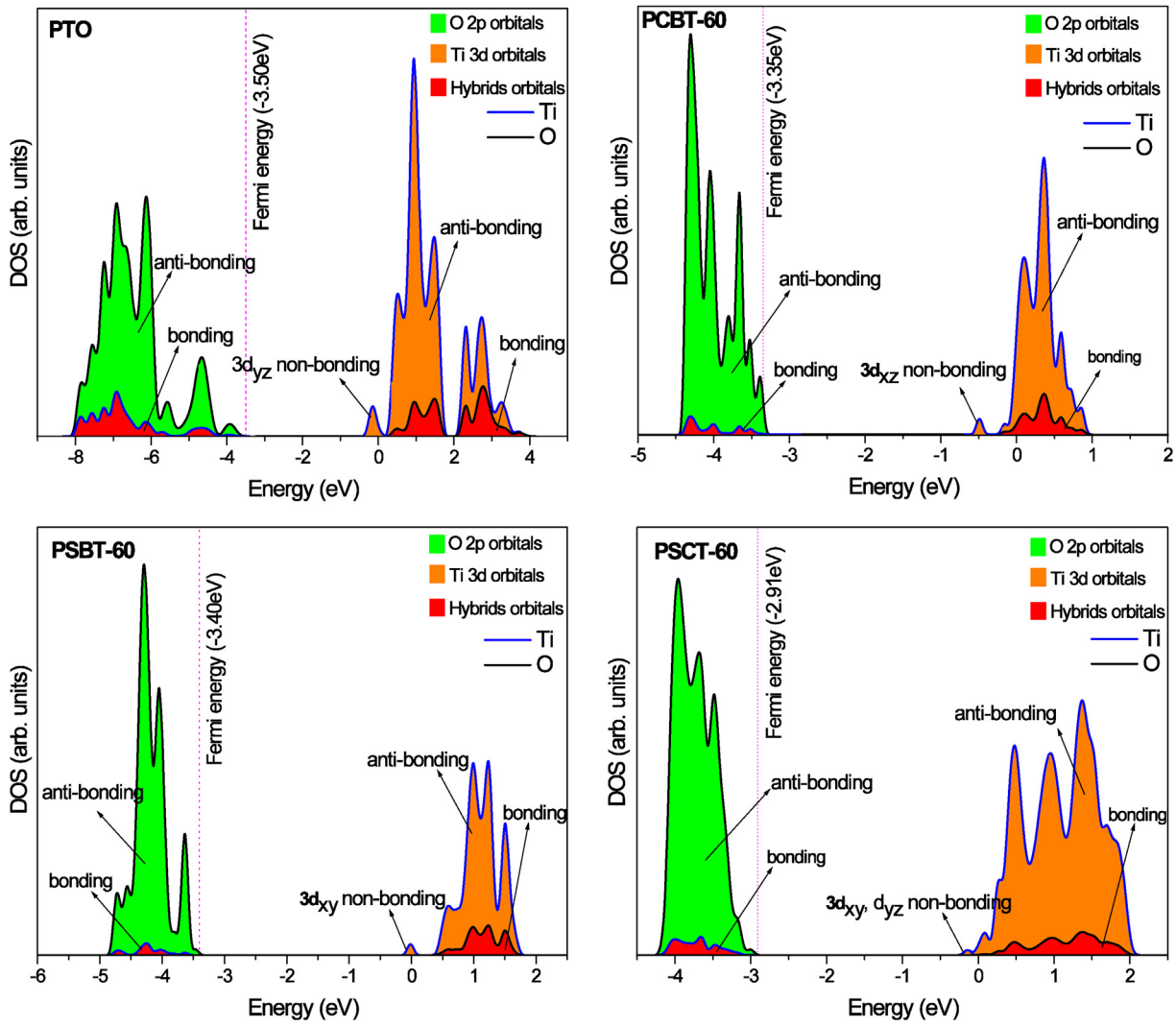

Fig. 9. Partial density of states (PDOS) projected for bonding, anti-bonding, and non-bonding orbitals of the O and Ti atoms in PTO, PCBT-60, PSBT-60, and PSCT-60 perovskite.

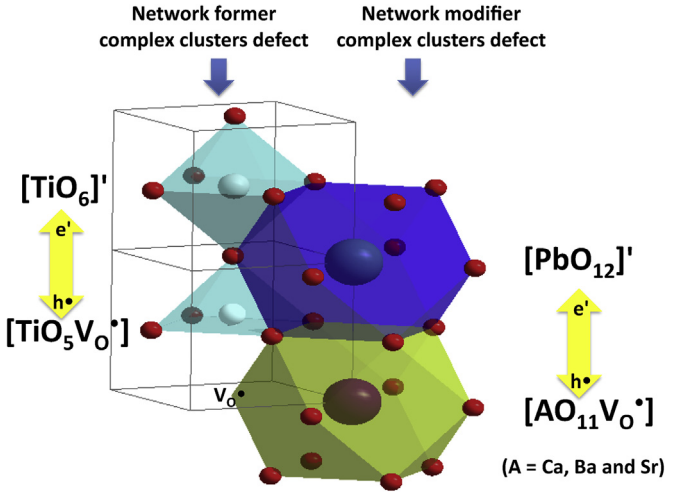

Fig. 10. A(A′A″)BO_3 perovskite structure, major structural distortions, and resulting electric dipole. The perovskite structure undergoes two major structural defects: network formed defects and network modifier defects. The combination of the charge motions on defects induces electric dipoles (Polarization), as indicated by yellow arrows. (For interpretation of the references to colour in this figure legend, the reader is referred to the web version of this article.)

Table 3
Calculated Mulliken charges for each individually clusters of PCBT-60, PSBT-60 and PSCT-60 compounds.

	$[TiO_5V_O^{\bullet}]$	$[TiO_6]'$	$[PbO_{12}]'$	$[CaO_{11}V_O^{\bullet}]$	$[BaO_{11}V_O^{\bullet}]$	$[SrO_{11}V_O^{\bullet}]$
PCBT-60	−1393	−1689	−2377	−2165	−2228	–
PSBT-60	−1257	−1604	−2296	–	−2160	−2106
PSCT-60	−1175	−1421	−2283	−2000	–	−1935

located between A to Γ, and 3.03 eV between X to Γ, for $PbTiO_3$, PCBT-60, PSBT-60, and PSCT-60 perovskite oxides, respectively. (vii) DFT results have demonstrated a strong correlation between overall ferroelectric responses at the nanoscale level of perovskite complex films and the strength of the Ti non-bonding orbitals participation. In cases where this participation (non-bonding orbitals) is especially weak, such as for the PSCT-60 sample, an unusually large enhancement of the ferroelectric instability was found.

The overall conclusion is that our first-principles DFT computational results are in good agreement with the PFM-based experimental results at the nanometer scale. This demonstrates that accurate density functional theory calculations can be used to identify properties of unexplored ABO_3 complex perovskite solid solutions.

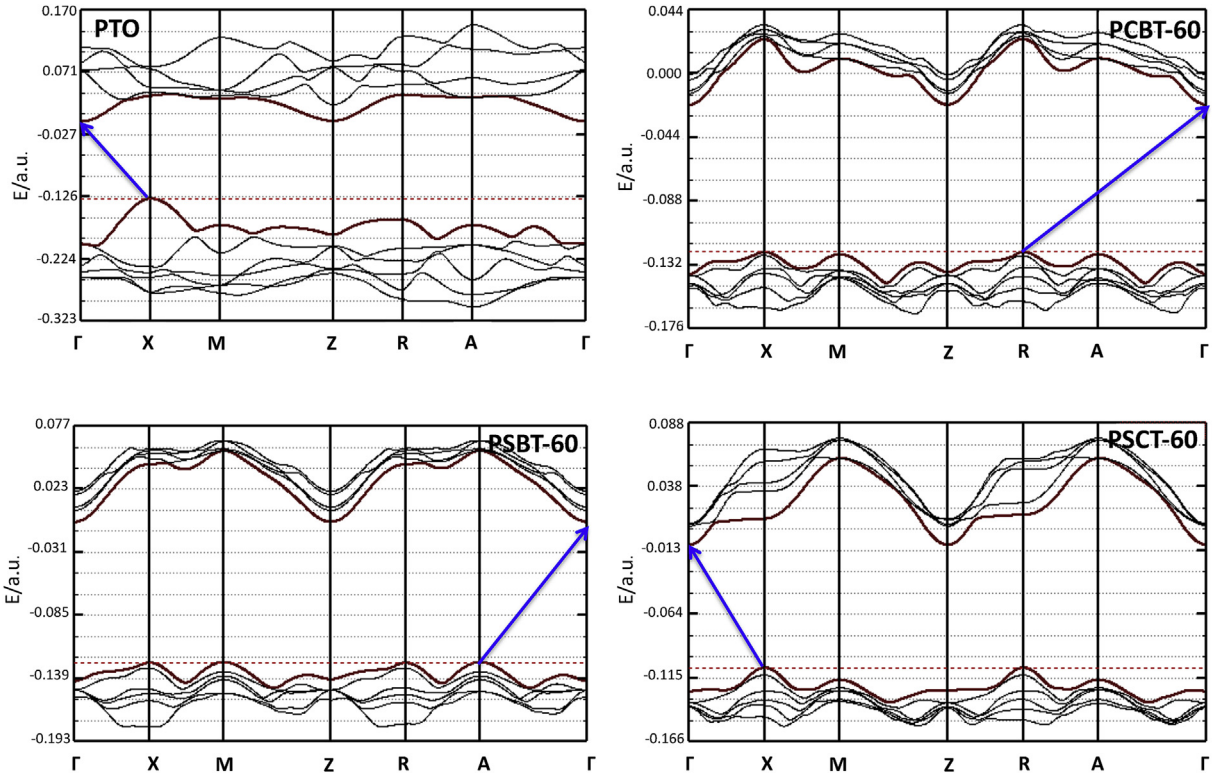

Fig. 11. Electronic band structure of PTO, PCBT-60, PSBT-60, and PSCT-60. The Fermi level is located at the top valence band as indicated by the horizontal dotted red line. The indirect band gap is indicated by solid blue arrows. (For interpretation of the references to colour in this figure legend, the reader is referred to the web version of this article.)

Acknowledgments

This study was financially supported by the Brazilian agencies FAPESP and CNPq. We would like to thank CEPID/CMDMC/INCTMN/CDMF, FAPESP (processes nº. 11/20536-7, 12/14106-2, and 13/07296-2) and CNPq (process nº. 470147/2012-1).

References

[1] T.S. Sherkar, L.J.A. Koster, Phys. Chem. Chem. Phys. 18 (2016) 331–338.
[2] D.A. Egger, A.M. Rappe, L. Kronik, ACC. Chem. Res. 49 (2016) 573.
[3] B. Chen, J. Shi, X. Zheng, Y. Zhou, K. Zhuc, S. Priya, J. Mater. Chem. A 3 (2015) 7699.
[4] X.F. Hao, A. Stroppa, P. Barone, A. Filippetti, C. Franchini, S. Picozzi, New J. Phys. 6 (2014) 015030.
[5] G. Dong, H. Fan, H. Tian, J. Fang, Q. Li, RSC Adv. 5 (2015) 29618.
[6] H. Wang, J. Wen, D.J. Miller, Q. Zhou, M. Chen, H.N. Lee, K.M. Rabe, X. Wu, Phys. Rev. X 8 (2016) 011027.
[7] C. He, Z.-J. Ma, B.-Z. Sun, R.-J. Sa, K. Wu, J. Alloys Compd. 623 (2015) 393.
[8] N. Pathak, S.K. Gupta, P.S. Ghosh, A. Arya, V. Natarajana, R.M. Kadama, RSC Adv. 5 (2015) 17501.
[9] H.-R. Fuh, Y.-P. Liu, S.-H. Chen, Y.-K. Wang, J. Alloys Compd. 547 (2013) 126.
[10] K.R. Tolman, R. Ubic, J. Alloys Compd. 690 (2017) 825.
[11] V.M. Longo, M.G.S. Costa, A.Z. Simões, I.L.V. Rosa, C.O.P. Santos, J. Andrés, E. Longo, J.A. Varela, Phys. Chem. Chem. Phys. 12 (2010) 7566.
[12] J.W. Bennett, I. Grinberg, A.M. Rappe, J. Am. Chem. Soc. 130 (2008) 17409.
[13] H. Ossmer, C. Slouka, L. Andrejs, P. Blaha, G. Friedbacher, J. Fleig, Solid State Ion. 281 (2015) 49.
[14] R.K. Kotnala, K.C. Verma, M.C. Mathpal, N.S. Negi, J. Phys. D: Appl. Phys. 42 (2009) 085408.
[15] M. Yashima, K. Omoto, J. Chen, H. Kato, X. Xing, Chem. Mater 23 (2011) 3135.
[16] F. Wang, L. Fan, Y. Ren, J. Chen, X. Xing, Appl. Phys. Lett. 104 (2014) 252901.
[17] J.A. Brehm, H. Takenaka, C.-W. Lee, I. Grinberg, J.W. Bennett, M.R. Schoenberg, A.M. Rappe, Phys. Rev. B 89 (2014) 195202.
[18] R.E. Cohen, Nature 358 (1992) 136.
[19] Y. Xu Wang, M. Arai, T. Sasaki, C.L. Wang, W.L. Zhong, Surf. Sci. 585 (2005) 75.
[20] S. Lazaro, E. Longo, J.R. Sambrano, A. Beltran, Surf. Sci. 552 (2004) 149.
[21] T. Shimada, X. Wang, Y. Kondo, T. Kitamura, Phys. Rev. Lett. 108 (2012) 067601.
[22] E.C. Paris, M.F.C. Gurgel, M.R. Joya, G.P. Casali, C.O. Paiva-Santos, T.M. Boschi, P.S. Pizani, J.A. Varela, E. Longo, J. Phys. Chem. Sol. 71 (2010) 12.
[23] G.Y. Gou, J.W. Bennett, H. Takenaka, A.M. Rappe, Phys. Rev. B 83 (2011) 205115.
[24] Z. Zhang, L. Lu, C. Shu, P. Wu, W. Song, J. Appl. Phys. 102 (2007) 074119.
[25] D. Lee, H. Lu, Y. Gu, S.-Y. Choi, S.-D. Li, S. Ryu, T.R. Paudel, K. Song, E. Mikheev, S. Lee, S. Stemmer, D.A. Tenne, S.H. Oh, E.Y. Tsymbal, X. Wu, L.-Q. Chen, A. Gruverman, C.B. Eom, Science 349 (2015) 1314.
[26] J. Seidel, L.W. Martin, Q. He, Q. Zhan, Y.H. Chu, A. Rother, M.E. Hawkridge, P. Maksymovych, P. Yu, M. Gajek, N. Balke, S.V. Kalinin, S. Gemming, F. Wang, G. Catalan, J.F. Scott, N.A. Spaldin, J. Orenstein, R. Ramesh, Nat. Mater 8 (2009) 229.
[27] F.M. Pontes, E.R. Leite, M.S.J. Nunes, D.S.L. Pontes, E. Longo, R. Magnani, P.S. Pizani, J.A. Varela, J. Eur. Ceram. Soc. 24 (2004) 2976.
[28] D.S.L. Pontes, F.M. Pontes, R.A. Capeli, M.L. Garzim, A.J. Chiquito, E. Longo, Ceram. Inter 40 (2014) 13363.
[29] J. Hlinka, P. Ondrejkovic, M. Kempa, E. Borissenko, M. Krisch, X. Long, Z.G. Ye, Phys. Rev. B Condens. Matter Mater. Phys. 83 (2011) 140101.
[30] A.D. Becke, J. Chem. Phys. 98 (1993) 5648.
[31] C.T. Lee, W.T. Yang, R.G. Parr, Phys. Rev. B 37 (1988) 785.
[32] N. Panwar, I. Coondoo, A. Tomar, A.L. Kholkin, V.S. Puli, R.S. Katiyar, Mat. Res. Bull. 47 (2012) 4240.
[33] D.V. Karpinsky, R.C. Pullar, Y.K. Fetisov, K.E. Kamentsev, A.L. Kholkin, J. Appl. Phys. 108 (2010) 042012.
[34] Y.X. Wang, M. Arai, T. Sasaki, C.L. Wang, W.L. Zhong, Surf. Sci. 585 (2005) 75.
[35] F. Wang, L. Fan, Y. Ren, J. Chen, X. Xing, Appl. Phys. Lett. 104 (2014) 252901.
[36] N. Choudhury, E.J. Walter, A.I. Kolesnikov, C.-K. Loong, Phys. Rev. B 77 (2008) 134111.
[37] L.H. Oliveira, E.C. Paris, W. Avansi, M.A. Ramirez, V.R. Mastelaro, E. Longo, J.A. Varela, J. Am. Ceram. Soc. 96 (2013) 209.
[38] R.A.P. Ribeiro, S.R. de Lázaro, RSC Adv. 4 (2014) 59839.
[39] N. Pathak, S.K. Gupta, P.S. Ghosh, A. Arya, V. Natarajana, R.M. Kadama, RSC Adv. 5 (2015) 17501.
[40] E. Silva Jr., F.A. La Porta, M.S. Liu, J. Andrés, J.A. Varela, E. Longo, Dalton Trans. 44 (2015) 3159.